to control the microenvironment of the nucleation site and to manipulate near-surface gradients of concentrations of the crystallizing ions by patterning SAMs into rapidly and slowly nucleating regions.

The technique we report here gives us the ability to fabricate a large number of indistinguishable active nucleation regions, and to nucleate one crystal in each region. This should enable the study of fundamental aspects of the crystallization process by providing access to statistically significant numbers of nucleation events in highly controlled microenvironments. □

Received 20 October 1998; accepted 29 January 1999.

1. Heuer, A. H. *et al.* Innovative materials processing strategies: A biomimetic approach. *Science* **255,** 1098–1105 (1992).
2. Stupp, S. I. & Braun, P. V. Molecular manipulation of microstructures: Biomaterials, ceramics, and semiconductors. *Science* **277,** 1242–1246 (1997).
3. Zelinsky, B. J. J., Brinker, C. J., Clark, D. E. & Ulrich, D. R. *Better Ceramics Through Chemistry* (Materials Research Soc., Pittsburgh, 1990).
4. Mann, S. & Ozin, G. A. Synthesis of inorganic materials with complex form. *Nature* **382,** 313–318 (1996).
5. Landau, E. M., Levanon, M., Leiserowitz, L., Lahav, M. & Sagiv, J. Transfer of structural information from Langmuir monolayers to three-dimensional growing crystals. *Nature* **318,** 353–356 (1985).
6. Addadi, L., Moradian, J., Shay, E., Maroudas, N. G. & Weiner, S. A chemical model for the cooperation of sulfates and carboxylates in calcite crystal nucleation: relevance to biomineralization. *Proc. Natl Acad. Sci. USA* **84,** 2732–2736 (1987).
7. Belcher, A. M. *et al.* Control of crystal phase switching and orientation by soluble molusc-shell proteins. *Nature* **381,** 56–58 (1996).
8. Alper, M., Calvert, P. D., Frankel, R., Rieke, P. C. & Tirrell, D. A. *Materials Synthesis Based on Biological Processes* (Materials Research Soc., Pittsburgh, 1991).
9. Mann, S. *et al.* Crystallisation at inorganic-organic interfaces: Biominerals and biomimetic synthesis. *Science* **261,** 1286–1292 (1993).
10. Mann, S. Molecular tectonics in biomineralization and biomimetic materials chemistry. *Nature* **365,** 499–505 (1993).
11. Mann, S., Heywood, B. R., Rajam, S. & Birchall, J. D. Controlled crystallisation of $CaCO_3$ under stearic acid monolayers. *Nature* **334,** 692–695 (1988).
12. Heywood, B. R. & Mann, S. Template-directed nucleation and growth of inorganic materials. *Adv. Mat.* **6,** 9–20 (1994).
13. Bunker, B. C. *et al.* Ceramic thin-film formation on functionalized interfaces through biomimetic processing. *Science* **264,** 48–55 (1994).
14. Aizenberg, J., Black, A. J. & Whitesides, G. M. Controlling local disorder in self-assembled monolayers by patterning the topography of their metallic supports. *Nature* **394,** 868–871 (1998).
15. Gupta, V. K. & Abbott, N. L. Design of surfaces for patterned alignment of liquid crystals on planar and curved substrates. *Science* **276,** 1533–1535 (1997).
16. Berman, A. *et al.* Total alignment of calcite at acidic polydiacetylene films: Cooperativity at the organic-inorganic interface. *Science* **269,** 515–518 (1995).
17. Laibinis, P. E. *et al.* Comparison of the structures and wetting properties of self-assembled monolayers of *n*-alkanethiols on the coinage metal surfaces, Cu, Ag, Au. *J. Am. Chem. Soc.* **113,** 7152–7167 (1991).
18. Kumar, A., Abbott, N. A., Kim, E., Biebuyck, H. A. & Whitesides, G. M. Patterned self-assembled monolayers and meso-scale phenomena. *Acc. Chem. Res.* **28,** 219–226 (1995).
19. Xia, Y. & Whitesides, G. M. Soft Lithography. *Angew. Chem. Int. Edn. Engl.* **37,** 550–575 (1998).
20. Lippmann, F. *Sedimentary Carbonate Minerals* (Springer, Berlin, 1973).
21. Lowenstam, H. A. & Weiner, S. *On Biomineralization* (Oxford Univ. Press, 1989).
22. Barabási, A.-L. & Stanley, H. E. *Fractal Concepts in Surface Growth* (Cambridge Univ. Press, 1995).

Acknowledgements. This work has been supported in part by the ONR and DARPA. It used MRSEC Shared Facilities supported by the NSF.

Correspondence and requests for materials should be addressed to G.M.W. (e-mail: gwhitesides@gmwgroup.harvard.edu) and J.A. (e-mail: jaizenberg@lucent.com).

Complete asymmetric induction of supramolecular chirality in a hydrogen-bonded assembly

Leonard J. Prins, Jurriaan Huskens, Feike de Jong, Peter Timmerman & David N. Reinhoudt

Laboratory of Supramolecular Chemistry and Technology, MESA⁺ Research Institute, University of Twente, PO Box 217, 7500 AE Enschede, The Netherlands

Chirality at the supramolecular level involves the non-symmetric arrangement of molecular components in a non-covalent assembly[1,2]. Supramolecular chirality is abundant in biology, for example in the DNA double helix[3], the triple helix of collagen[4] and the α-helical coiled coil of myosin[5]. These structures are stabilized by inter-strand hydrogen bonds, and their handedness is determined by the configuration of chiral centres in the nucleotide or peptide backbone. Synthetic hydrogen-bonded assemblies have been reported that display supramolecular chirality in solution[6–8] or in the solid state[9–12]. Complete asymmetric induction of supramolecular chirality—the formation of assemblies of a single handedness—has been widely studied in polymeric superstructures[13,14]. It has so far been achieved in inorganic metal-coordinated systems[15–17], but not in organic hydrogen-bonded assemblies[18–20]. Here we describe the diastereoselective assembly of enantio-pure calix[4]arene dimelamines and 5,5-diethylbarbituric acid (DEB) into chiral hydrogen-bonded structures of one handedness. The system displays complete enantioselective self-resolution: the mixing of homomeric assemblies (composed of homochiral units) with opposite handedness does not lead to the formation of heteromeric assemblies. The non-covalent character of the chiral assemblies, the structural simplicity of the constituent building blocks and the ability to control the assembly process by means of peripheral chiral centres makes this system promising for the development of a wide range of homochiral supramolecular materials or enantioselective catalysts.

Previously we have shown by X-ray crystallography and ^{1}H NMR spectroscopy that assembly $\mathbf{1}_3$•DEB_6 exclusively forms as the staggered isomer **A** (D_3), which displays supramolecular chirality both in solution and in the solid state (see Fig. 1)[21,22]. In the absence of any other source of chirality, this isomer exists as a racemic mixture of the *M*- and *P*-enantiomers.

We have now found that assembly of 3 equivalents of the chiral calix[4]arene dimelamines (*R*,*R*)-**2** or (*S*,*S*)-**3**, having (*R*)- or (*S*)-1-phenylethylamine moieties, respectively, with 6 equivalents of DEB gives quantitatively the assemblies $\mathbf{2}_3$•DEB_6 (*M*-enantiomer) or $\mathbf{3}_3$•DEB_6 (*P*-enantiomer) (compounds **1**–**7** are shown in Fig. 1). The induction of helicity in both assemblies is complete (d.e. > 98%, where d.e. is diastereomeric excess) as judged from the single set of signals in the ^{1}H NMR spectra (CD_2Cl_2) (Fig. 2). None of the other possible diastereoisomeric assemblies (that is, (*P*)-$\mathbf{2}_3$•DEB_6 and (*M*)-$\mathbf{3}_3$•DEB_6) is present. Two-dimensional rotating frame Overhauser effect spectroscopy (ROESY) experiments correlate the absolute configuration of the substituents with the helicity: an (*R*)-substituent induces *M*-helicity, and an (*S*)-substituent induces *P*-helicity, in the assembly (Fig. 2d). We note that both assemblies are strongly active in circular dichroism (CD; $\Delta\epsilon_{max} \approx 100\,cm^2\,mmol^{-1}$, where $\Delta\epsilon_{max} = (\epsilon_L - \epsilon_R)_{286\,nm}$, Fig. 3a), while none of the individual components (*R*,*R*)-**2** or (*S*,*S*)-**3** show any significant CD activity ($\Delta\epsilon_{max} < 8\,cm^2\,mmol^{-1}$). The observed CD is thus clearly a direct result of assembly formation and not an intrinsic property of the individual components.

Complete induction of chirality was also observed for the (*S*)-alanine- and (*R*)-naphthyldimelamine assemblies (*P*)-$\mathbf{4}_3$•DEB_6 and (*M*)-$\mathbf{5}_3$•DEB_6 (d.e. > 98% according to ^{1}H NMR spectroscopy; data not shown) and seems to be a general phenomenon for this type of assembly. Moreover, complete chiral induction is also observed with peripheral chiral centres in the cyanurate components. Combination of achiral dimelamine **6** with chiral cyanurates (*R*)- or (*S*)-MePhCYA or amino acid-derived cyanurates (*S*)-PheCYA, (*S*)-ValCYA, or (*S*)-LeuCYA (see Fig. 1 for nomenclature) leads in all cases to diastereoselective assembly of $\mathbf{6}_3$•CYA_6 with d.e. values >98% according to ^{1}H NMR spectroscopy (data not shown). The CD spectra of the assemblies $\mathbf{2}_3$•DEB_6–$\mathbf{5}_3$•DEB_6 and $\mathbf{6}_3$•CYA_6 all display bisignate curves with remarkably large amplitudes. The peripheral chromophores (benzyl, carbonyl, naphthyl) only affect the intensity of the Cotton effect (CE) at lower wavelengths, while the CD curves are virtually identical above 250 nm (Fig. 3). The observed Cotton effects seem to be largely the result of exciton coupling between chromophores present in the core of the assemblies. Comparison of the different CD spectra suggests that the sign of the CD curve is a good probe for the helicity of the assembly.

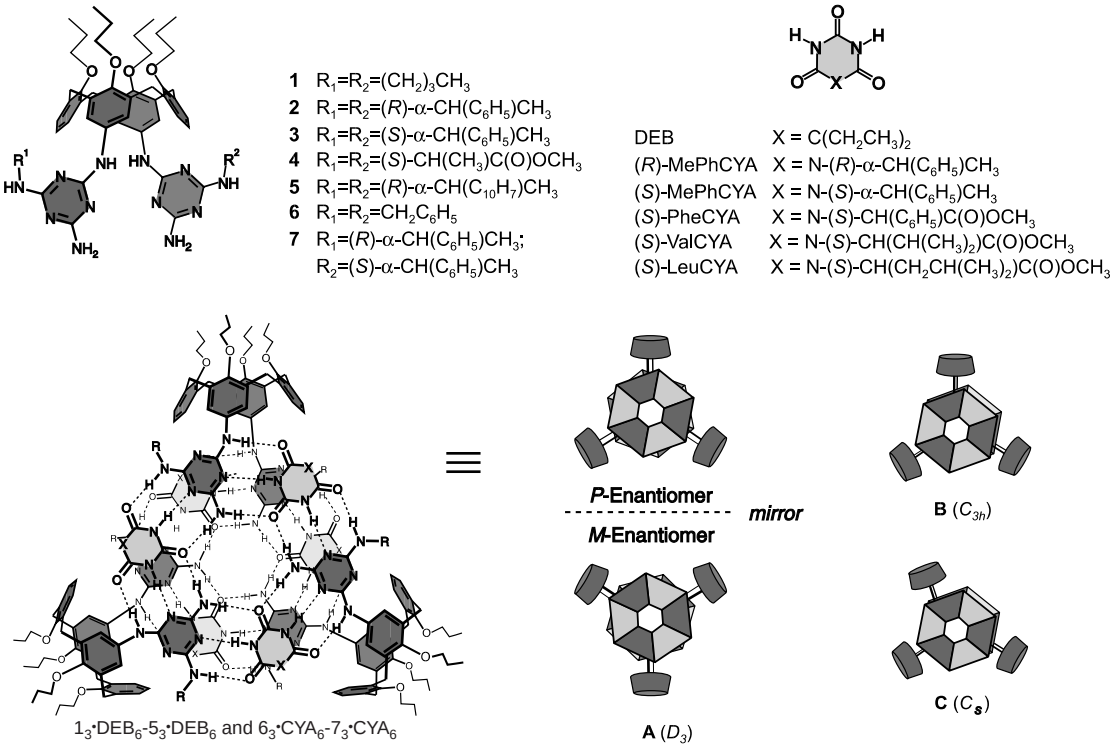

Figure 1 Schematic representations and molecular structure of the nine-component hydrogen bonded assemblies $\mathbf{1}_3$•DEB_6–$\mathbf{5}_3$•DEB_6, $\mathbf{6}_3$•CYA_6 and $\mathbf{7}_3$•CYA_6 with their individual components. The assemblies can exist in three isomeric forms: the chiral staggered isomer **A** (D_3 symmetry), and the achiral eclipsed isomers **B** (C_{3h} symmetry) and **C** (C_s symmetry). The chiral isomer **A** can be present as a mixture of the *P*- and *M*-enantiomer. The assignment of the *M*/*P*-configuration is based on a clockwise (*P*) or anticlockwise (*M*) orientation of the two melamine units in the assembly[27].

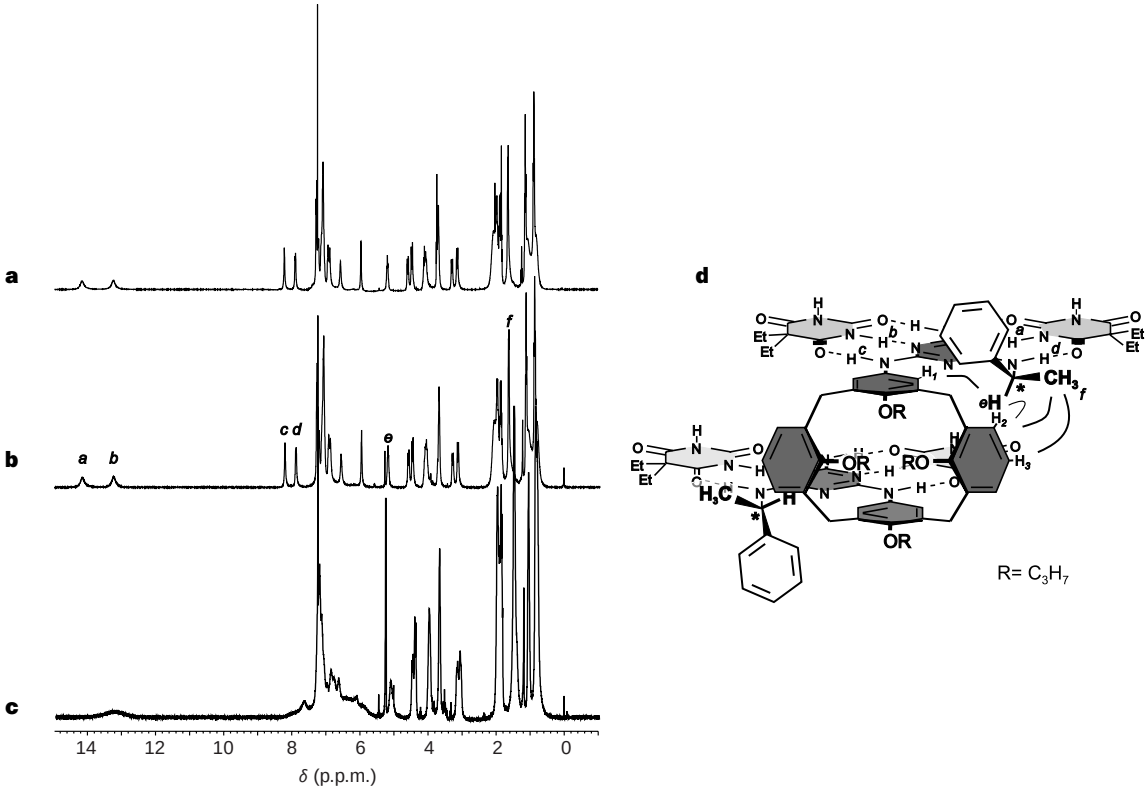

Figure 2 Characterization of chiral non-covalent assemblies (*M*)-$\mathbf{2}_3$•DEB_6 and (*P*)-$\mathbf{3}_3$•DEB_6 by ^{1}H NMR spectroscopy. **a**, 400 MHz spectrum of enantiomerically pure assembly (*M*)-$\mathbf{2}_3$•DEB_6; **b**, 400 MHz spectrum of enantiomerically pure assembly (*P*)-$\mathbf{3}_3$•DEB_6; **c**, 400 MHz spectrum of the assembly of (*R*,*S*)-**7** and DEB (2 equiv.); all spectra were recorded in CD_2Cl_2 (1 mM) at 298 K relative to residual $CHDCl_2$. **d**, 2D ROESY connectivities measured for assembly (*P*)-$\mathbf{3}_3$•DEB_6 in toluene-d_8. Medium connectivities were observed for the following protons: H_e and H_1, H_e and H_2, H_f and H_2, and H_f and H_3. These connectivities relate the configuration of the chiral substituent (*S*) with the helicity (*P*) of the assembly. Additional evidence for the formation of assemblies (*M*)-$\mathbf{2}_3$•DEB_6 and (*P*)-$\mathbf{3}_3$•DEB_6 was obtained by MALDI-TOF mass spectrometry using Ag^+-labelling[28]. Both assemblies exhibit a strong signal at *m/z* 4,358.3 (calculated for $C_{234}H_{288}N_{48}O_{30}$•$^{107}Ag^+$, 4,360.2) corresponding to the monovalent Ag^+-complexes.

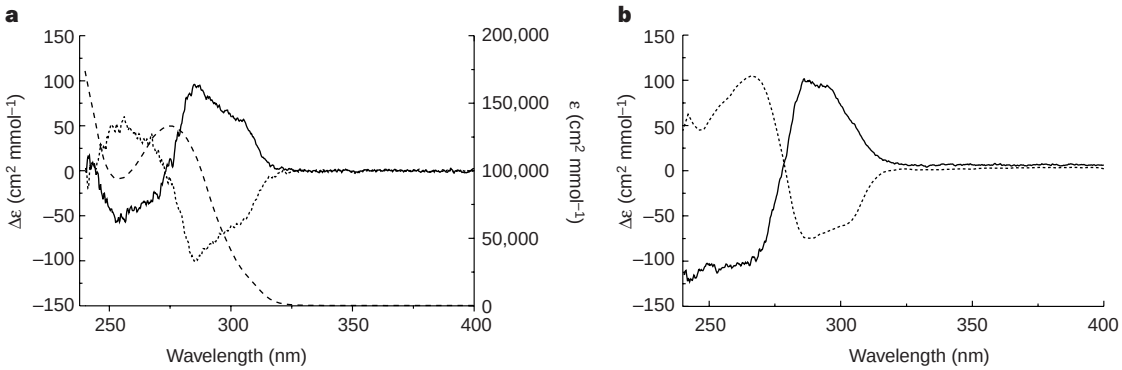

Figure 3 Characterization of assemblies $\mathbf{2}_3$•DEB_6–$\mathbf{5}_3$•DEB_6 by CD and ultraviolet spectroscopy. **a**, CD spectra and ultraviolet spectrum (dashed line) of enantiomerically pure assemblies (*M*)-$\mathbf{2}_3$•DEB_6 (solid) and (*P*)-$\mathbf{3}_3$•DEB_6 (dotted); **b**, CD spectra of enantiomerically pure assemblies (*P*)-$\mathbf{4}_3$•DEB_6 (dotted) and (*M*)-$\mathbf{5}_3$•DEB_6 (solid). Spectra were recorded in CH_2Cl_2 (1 mM) at 298 K.

The observed induction of supramolecular chirality is obviously related to the presence of six peripheral chiral centres in each assembly. The energy parameters for the chirality induction were determined using a theoretical model in which the difference in enthalpy between the *M*- and *P*-helix (ΔH_{total}) is regarded as the sum of six individual contributions of each chiral centre ($\Delta H_{R/S}$) (see Supplementary Information). Using this model, the values of ΔH_{total} and $\Delta H_{R/S}$ can be determined directly from the measured d.e. values via the relation: $\Delta H_{total} = 6\Delta H_{R/S} = -RT\ln[-(\text{d.e.}_{6R}+100)/(\text{d.e.}_{6R}-100)]$, where d.e._{6R} is the diastereomeric excess in an assembly with 6 (*R*)-substituents. For example, a $\text{d.e.}_{6R} > 98\%$ gives $-\Delta H_{total}(298\,K) > 11.4\,kJ\,mol^{-1}$ and $-\Delta H_{R/S}(298\,K) > 1.90\,kJ\,mol^{-1}$. Cooperativity between the chiral centres is not included in the model, but will lead to the fact that $-\Delta H_{R/S} < -\Delta H_{total}/6$.

For a more accurate determination of $\Delta H_{R/S}$, we studied the heteromeric assemblies $\mathbf{2}_{3-n}\mathbf{6}_n$•$DEB_6$ ($n = 1$–2), in which 1 or 2 chiral components (*R*,*R*)-**2** are replaced by achiral components **6**. Determination of the corresponding d.e. values ($\text{d.e.}_{4R/2N}$ and $\text{d.e.}_{2R/4N}$)—which will be lower than d.e._{6R} as a result of the reduced number of chiral centres—will therefore allow a more accurate determination of $\Delta H_{R/S}$. The heteromeric assemblies $\mathbf{2}_{3-n}\mathbf{6}_n$•$DEB_6$ ($n = 1$–2) cannot be obtained in pure form due to their dynamic character, but are formed spontaneously by mixing the homomeric assemblies (*M*)-$\mathbf{2}_3$•DEB_6 (Fig. 4a) and $\mathbf{6}_3$•DEB_6 (Fig. 4b), as indicated by multiple signals in the ^{1}H NMR spectrum (Fig. 4c). We have shown previously that mixtures of achiral assemblies have a statistical composition[23]. Titration of chiral assembly (*M*)-$\mathbf{2}_3$•DEB_6 with racemic assembly $\mathbf{6}_3$•DEB_6 followed by measurement of the CD spectra reveals a nonlinear relation between the chiroptical activity ($\Delta\epsilon_{286}$) of the mixture and the amount of added $\mathbf{6}_3$•DEB_6 (Fig. 4d). The chiroptical activity for each measurement is composed of three individual contributions: $\Delta\epsilon_{total} = (\text{d.e.}_{6R}[\mathbf{2}_3\text{•}DEB_6] + \text{d.e.}_{4R/2N}[\mathbf{2}_2\mathbf{6}\text{•}DEB_6] + \text{d.e.}_{2R/4N}[\mathbf{26}_2\text{•}DEB_6])/(\Sigma_{(n=0-3)}[\mathbf{2}_{3-n}\mathbf{6}_n\text{•}DEB_6]) \times \Delta\epsilon(\mathbf{2}_3\text{•}DEB_6)$, assuming the same $\Delta\epsilon$ for each assembly $\mathbf{2}_{3-n}\mathbf{6}_n$•$DEB_6$ ($n = 0$–3). Curve fitting (see Supplementary Information) using the theoretical model described above reveals the best fit for $-\Delta H_{total}(298\,K) = 13.4\,kJ\,mol^{-1}$ and $-\Delta H_{R/S}(298\,K) = 2.23\,kJ\,mol^{-1}$ (Fig. 4d), with corresponding d.e. values of 99.1% ($\mathbf{2}_3$•DEB_6), 94.7% ($\mathbf{2}_2\mathbf{6}$•DEB_6) and 71.7% ($\mathbf{26}_2$•DEB_6). The d.e._{6R} value of 99.1% for assembly (*M*)-$\mathbf{2}_3$•DEB_6 is in good agreement with that determined by ^{1}H NMR spectroscopy (see above). The chirality induction in the heteromeric assemblies $\mathbf{2}_{3-n}\mathbf{6}_n$•$DEB_6$ ($n = 1$–2) resembles the 'Sergeants and Soldiers' principle (that is, the achiral units reinforce the induced chirality of the chiral units) as observed previously in polymeric[24] and liquid crystalline[14] materials.

We also investigated mixtures of the chiral assemblies (*M*)-$\mathbf{2}_3$•DEB_6 and (*P*)-$\mathbf{3}_3$•DEB_6. The ^{1}H NMR spectrum of a 1:1 mixture of the assemblies is identical to that of the separate assemblies (Fig. 5a–c). Additional signals are not observed, which indicates that the heteromeric assemblies $\mathbf{2}_{3-n}\mathbf{3}_n$•$DEB_6$ ($n = 1$–2) are not formed to a significant extent. Moreover, titration of (*M*)-$\mathbf{2}_3$•DEB_6 with (*P*)-$\mathbf{3}_3$•DEB_6 followed by CD shows a strictly

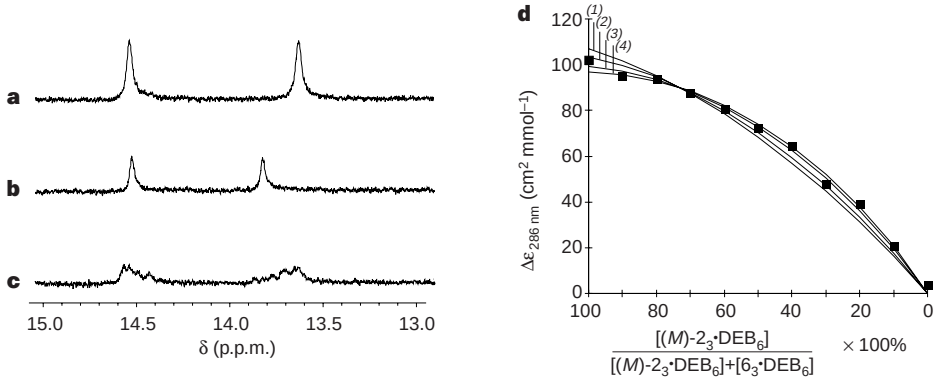

Figure 4 Characterization of mixed assemblies $\mathbf{2}_{3-n}\mathbf{6}_n$•$DEB_6$ ($n = 0$–3) by ^{1}H NMR and CD spectroscopy. The figure shows the 13–15 p.p.m. region of the 300 MHz ^{1}H NMR spectrum of: **a**, enantiomerically pure assembly (*M*)-$\mathbf{2}_3$•DEB_6; **b**, racemic assembly $\mathbf{6}_3$•DEB_6; and **c**, a 1:1 mixture of (*M*)-$\mathbf{2}_3$•DEB_6 and $\mathbf{6}_3$•DEB_6. All spectra were recorded in toluene-d_8 (1 mM) at 298 K relative to residual $C_6D_5CHD_2$. **d**, Plot of the CD intensity (filled squares, measured at 286 nm) versus the ratio [(*M*)-$\mathbf{2}_3$•DEB_6]/([(*M*)-$\mathbf{2}_3$•DEB_6] + [$\mathbf{6}_3$•DEB_6]) × 100%. The lines represent the calculated curves for $\Delta H_{total} = -8.0$(*1*), –10.0(*2*), –13.4 (*3*, best fit) and –16.0 (*4*) kJ mol^{-1}.

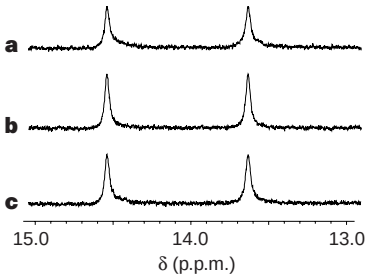

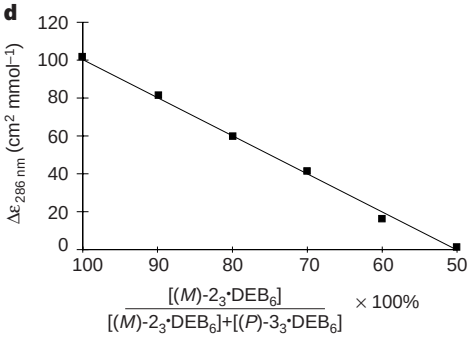

Figure 5 Characterization of mixed assemblies $\mathbf{2}_{3-n}\mathbf{3}_n$•$DEB_6$ ($n = 0$–3) by ^{1}H NMR and CD spectroscopy. The figure shows the 13–15 p.p.m. region of the 300 MHz ^{1}H NMR spectrum of: **a**, enantiomerically pure assembly (*M*)-$\mathbf{2}_3$•DEB_6; **b**, enantiomerically pure assembly (*P*)-$\mathbf{3}_3$•DEB_6; and **c**, a 1:1 mixture of (*M*)-$\mathbf{2}_3$•DEB_6 and (*P*)-$\mathbf{3}_3$•DEB_6. All spectra were recorded in toluene-d_8 (1 mM) at 298 K. **d**, Plot of the CD intensity (filled squares, measured at 286 nm) versus the ratio $[(M)\text{-}\mathbf{2}_3\text{•}DEB_6]/([(M)\text{-}\mathbf{2}_3\text{•}DEB_6] + [(P)\text{-}\mathbf{3}_3\text{•}DEB_6]) \times 100\%$. The solid line represents the calculated curve for $\Delta H_{total} = -15.0\ kJ\ mol^{-1}$.

linear decrease of the chiroptical activity (Fig. 5d). Curve fitting (see Supplementary Information) using the theoretical model reveals an improving fit for increasing $-\Delta H_{R/S}$ values. These results confirm the ^{1}H NMR experiment, and also indicate that the homomeric assemblies (*M*)-$\mathbf{2}_3$•DEB_6 and (*P*)-$\mathbf{3}_3$•DEB_6 are exclusively present in a mixture of the chiral building blocks (*R*,*R*)-**2** and (*S*,*S*)-**3** and DEB (3:3:6). In the case of statistical mixing, a 25:75 mixture of homomeric and heteromeric assemblies would be formed. The present system thus constitutes an example of complete enantioselective self-resolution in a dynamic hydrogen-bonded assembly in solution, a phenomenon so far only observed for hydrogen-bonded assemblies in the solid[25] or liquid-crystalline[26] state.

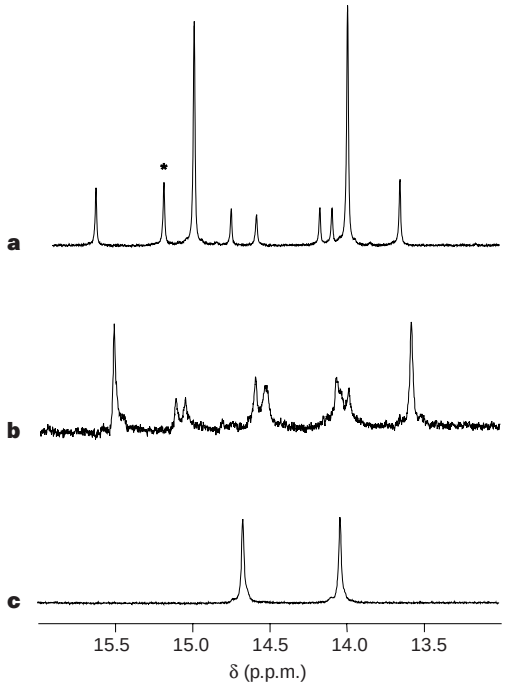

Figure 6 Isomeric distribution of hydrogen-bonded assemblies from **1**, (*R*,*R*)-**2**, and (*R*,*S*)-**7** with HexCYA as determined by ^{1}H NMR spectroscopy. 300 MHz ^{1}H NMR spectrum (13–16 p.p.m.) of: **a**, assembly $\mathbf{1}_3$•$HexCYA_6$ (mixture of isomers **A**–**C**; the signal denoted with an asterisk represents two chemically different protons); **b**, *meso*-assembly $\mathbf{7}_3$•$HexCYA_6$ (mixture of isomers **B** and **C**); and **c**, enantiomerically pure assembly (*M*)-$\mathbf{2}_3$•$HexCYA_6$ (exclusive formation of isomer **A**). Additional evidence for the formation of assemblies (*M*)-$\mathbf{2}_3$•$HexCYA_6$ and $\mathbf{7}_3$•$HexCYA_6$ was obtained by MALDI-TOF mass spectrometry using Ag^+-labelling[28]. Both assemblies exhibit a strong signal at *m/z* 4,536.4 (calculated for $C_{240}H_{306}N_{54}O_{30}$•$^{107}Ag^+$, 4,535) corresponding to the monovalent Ag^+-complexes.

Chiral information in the individual components can also be used to control the conformation of the assembly. As we have shown above, both (*R*,*R*)-**2** and (*S*,*S*)-**3**, which have two chiral centres of identical configuration, preferentially assemble with DEB as the staggered isomer **A** (Fig. 1). In sharp contrast to this, dimelamine (*R*,*S*)-**7**, which has two chiral centres of opposite configuration, is not able to form isomer **A** in the presence of 2 equivalents of DEB. In this case, non-defined oligomeric assemblies are formed that show broad signals in the ^{1}H NMR spectrum (Fig. 2c). More informative are the results obtained from assembly studies of **1**, (*R*,*R*)-**2**, and (*R*,*S*)-**7** with HexCYA. Assembly $\mathbf{1}_3$•$HexCYA_6$ exists as a mixture of isomer **A** (D_3) and the two achiral eclipsed isomers **B** (C_{3h}) and **C** (C_s) (Fig. 1). The ^{1}H NMR spectrum exhibits 10 different signals in the 14–16 p.p.m. region; that is, two signals each for **A** and **B**, and six signals for **C** (Fig. 6a). However, for (*R*,*R*)-**2** and (*R*,*S*)-**7** the isomeric distribution of the assembly with HexCYA is changed dramatically. Assembly of 3 equivalents of (*R*,*S*)-**7** with 6 equivalents of HexCYA gives a mixture of the two eclipsed isomers **B** and **C**. The ^{1}H NMR spectrum shows only eight signals in the 14–16 p.p.m. region, and isomer **A** is not present (Fig. 6b). In contrast to this, assembly of 3 equivalents of (*R*,*R*)-**2** and 6 equivalents of HexCYA gives isomer **A** as the only product. Not a trace of the isomers **B** and **C** is found in the ^{1}H NMR spectrum; there are only two signals in the 14–16 p.p.m. region (Fig. 6c). Assembly $\mathbf{2}_3$•$HexCYA_6$ exhibits a CD spectrum characteristic of assemblies of the isomer **A** type. These experiments again illustrate the decisive role that the peripheral chiral centres play in the assembly process. □

Methods

Hydrogen-bonded assemblies were prepared by suspending calix[4]arene dimelamines **1**–**7** and either DEB or CYA in a 1:2 molar ratio in toluene or CH_2Cl_2. Clear solutions were obtained after stirring the mixtures for 15 min at room temperature. Occasionally sonication or heating was required to dissolve the components. For the CD-titration experiments 1 mM solutions of the homomeric assemblies in CH_2Cl_2 were mixed in ratios of 10:1 to 1:10 for (*M*)-$\mathbf{2}_3$•DEB_6 and $\mathbf{6}_3$•DEB_6 and 10:1 to 5:5 for (*M*)-$\mathbf{2}_3$•DEB_6 and (*P*)-$\mathbf{3}_3$•DEB_6. The CD spectra were recorded 15 min after mixing the separate solutions.

Received 12 November 1998; accepted 2 February 1999.

1. Havinga, E. Spontaneous formation of optically active substances. *Biochim. Biophys. Acta* **13,** 171–174 (1954).
2. Lehn, J.-M. *Supramolecular Chemistry, Concepts and Perspectives* (VCH, Weinheim, 1995).
3. Dickerson, R. E. *et al*. The anatomy of A-, B-, and Z-DNA. *Science* **216,** 475–485 (1982).
4. Okuyama, K., Okuyama, K., Arnott, S., Takanyanagi, M. & Kakudo, M. Crystal and molecular structure of a collagen-like polypeptide (Pro-Pro-Gly)$_{10}$. *J. Mol. Biol.* **152,** 427–443 (1981).
5. Warrick, H. M. & Spudich, J. A. Myosin: structure and function in cell motility. *Annu. Rev. Cell Biol.* **3,** 379–422 (1987).
6. Seto, C. T. & Whitesides, G. M. Molecular self-assembly through hydrogen bonding: supramolecular aggregates based on the cyanuric acid.melamine lattice. *J. Am. Chem. Soc.* **115,** 905–916 (1993).

7. Ghadiri, M. R., Granja, J. R., Milligan, R. A., McRee, D. E. & Khazanovich, N. Self-assembling organic nanotubes based on a cyclic peptide architecture. *Nature* **366,** 324–327 (1993).
8. Conn, M. M. & Rebek, J. Jr Self-assembling capsules. *Chem. Rev.* **97,** 1647–1668 (1997).
9. Geib, S. J., Vincent, C., Fan, E. & Hamilton, A. D. A self-assembling, hydrogen-bonded helix. *Angew. Chem. Int. Edn Engl.* **32,** 119–121 (1993).
10. Hanessian, S., Gomtsyan, A., Simard, M. & Roelens, S. Molecular recognition and self-assembly by "weak" hydrogen bonding: unprecedented supramolecular helicate structures from diamine/diol motifs. *J. Am. Chem. Soc.* **116,** 4495–4496 (1994).
11. Saurez, M., Branda, N., Lehn, J.-M., De Cian, A. & Fischer, J. Supramolecular chirality: chiral hydrogen-bonded supermolecules from achiral molecular components. *Helv. Chim. Acta* **81,** 1–13 (1998).
12. Atwood, J. L. & MacGillivray, L. R. A chiral spherical molecular assembly held together by 60 hydrogen bonds. *Nature* **389,** 469–472 (1997).
13. Rowan, A. E. & Nolte, R. J. M. Helical molecular programming. *Angew. Chem. Int. Edn Engl.* **37,** 63–68 (1998).
14. Palmans, A. R. A., Vekemans, J. A. J. M., Havinga, E. E. & Meijer, E. W. Sergeants-and-soldiers principle in chiral columnar stacks of disc-shaped molecules with C_3 symmetry. *Angew. Chem. Int. Edn Engl.* **36,** 2648–2651 (1997).
15. Zarges, W., Hall, J., Lehn, J.-M. & Bolm, C. Helicity induction in helicate self-organisation from chiral tris(bipyridine) ligand strands. *Helv. Chim. Acta* **74,** 1843–1852 (1991).
16. Woods, C. R., Benaglia, M., Cozzi, F. & Siegel, J. S. Enantioselective synthesis of copper(I) bipyridine based helicates by chiral templating of secondary structure: transmission of stereochemistry on the nanometer scale. *Angew. Chem. Int. Edn Engl.* **35,** 1830–1833 (1996).
17. Mamula, O., Von Zelewsky, A. & Bernardinelli, G. Completely stereospecific self-assembly of a circular helicate. *Angew. Chem. Int. Edn Engl.* **37,** 289–293 (1998).
18. Castellano, R. K., Kim, B. H. & Rebek, J. Jr Chiral capsules: asymmetric binding in calixarene-based dimers. *J. Am. Chem. Soc.* **119,** 12671–12672 (1997).
19. Qiao, S., Choi, I. S. & Whitesides, G. M. Observation of diastereomers of the hydrogen-bonded aggregate Hub(M)$_3$.3CA using ^{1}H NMR spectroscopy when CA is an optically-active isocyanuric acid. *J. Org. Chem.* **62,** 2619–2621 (1997).
20. Rivera, J. M., Martin, T. & Rebek, J. Jr Chiral spaces: dissymmetric capsules through self-assembly. *Science* **279,** 1021–1023 (1998).
21. Vreekamp, R. H., Van Duynhoven, J. P. M., Hubert, M., Verboom, W. & Reinhoudt, D. N. Molecular boxes based on calix[4]arene double rosettes. *Angew. Chem. Int. Edn Engl.* **35,** 1215–1218 (1996).
22. Timmerman, P. *et al.* Noncovalent assembly of functional groups on calix[4]arene molecular boxes. *Chem. Eur. J.* **3,** 1823–1832 (1997).
23. Crego Calama, M., Fokkens, R., Nibbering, N. M. M., Timmerman, P. & Reinhoudt, D. N. Libraries of non-covalent hydrogen bonded assemblies; combinatorial synthesis of supramolecular systems. *Chem. Commun.* 1021–1022 (1998).
24. Green, M. M. *et al.* A helical polymer with a cooperative response to chiral information. *Science* **268,** 1860–1866 (1995).
25. Russell, K. C., Lehn, J.-M., Kyritsakas, N., DeCian, A. & Fischer, J. Self-assembly of hydrogen-bonded supramolecular strands from complementary melamine and barbiturate components with chiral selection. *New J. Chem.* **22,** 123–128 (1998).
26. Gulik-Krzywicki, T., Fouquey, C. & Lehn, J.-M. Electron microscopic study of supramolecular liquid crystalline polymers formed by molecular recognition-directed self-assembly from complementary chiral components. *Proc. Natl Acad. Sci. USA* **90,** 163–167 (1993).
27. Prelog, V. & Helmchen, G. Basis of the CIP system and proposal for a revision. *Angew. Chem. Int. Edn Engl.* **21,** 567–594 (1982).
28. Jolliffe, K. A. *et al.* Characterization of supramolecular hydrogen-bonded assemblies by MALDI-TOF mass spectrometry after Ag^+-labelling. *Angew. Chem. Int. Edn Engl.* **37,** 1294–1297 (1998).

Supplementary information is available on *Nature*'s World-Wide Web site (http://www.nature.com) or as paper copy from the London editorial office of *Nature*.

Acknowledgements. We thank R. Hulst for the 2D ROESY experiments, R. Fokkens and N. M. M. Nibbering for the MALDI-TOF measurements, and E. W. Meijer for providing the use of the CD equipment. This work was supported by the Council for Chemical Sciences (CW) and the Technology Foundation (STW) of the Netherlands Organization for Scientific Research (NWO).

Correspondence and requests for materials should be addressed to D.N.R. (e-mail: smct@ct.utwente.nl).

Variability of inorganic and organic phosphorus turnover rates in the coastal ocean

Claudia R. Benitez-Nelson & Ken O. Buesseler

Woods Hole Oceanographic Institution, Woods Hole, Massachusetts 02543, USA

Phosphorus is an essential nutrient in pelagic marine ecosystems. Phosphorus cycling in the upper ocean is, however, poorly understood, and few studies have directly investigated the biological utilization of this essential element[1–4]. Here, we have determined *in situ* phosphorus-turnover rates in a coastal marine environment by measuring the activities of two cosmogenic radionuclides (^{32}P and ^{33}P, with half lives of 14.3 and 25.3 days, respectively) in dissolved inorganic, dissolved organic and total particulate phosphorus pools over a seasonal cycle. Phosphorus turnover rates within dissolved and particulate pools are rapid and vary over seasonal timescales, suggesting that low phosphorus concentrations can support relatively high primary production. Furthermore, picoplankton, such as bacteria, appear preferentially to utilize certain dissolved organic phosphorus compounds to obtain other associated nutrients, such as carbon and nitrogen. It seems that the significance of the roles of both dissolved inorganic and organic phosphorus in supporting primary production—and, hence, CO_2 uptake and particulate organic carbon export—has been hitherto underestimated.

The radionuclides ^{32}P and ^{33}P are produced primarily by cosmic ray interactions with atmospheric argon and enter the oceans predominantly in rain[5–7]. If the ratio of ^{33}P/^{32}P in rain is known, then one can determine the relative 'age' of cosmogenic phosphorus, P, by measuring the ^{33}P/^{32}P ratio in various biological pools. High ^{33}P/^{32}P ratios indicate an older P pool. The inventories of ^{32}P and ^{33}P in the ocean are quite low, ranging from just tens to hundreds of disintegrations per minute per square metre (d.p.m. m^{-2})[1,8–10]. Thus, ^{32}P and ^{33}P measurements require several thousand litres of sea water and extensive purification from other β-emitters. Previous investigations which sought to utilize these isotopes were hampered by a lack of known input fluxes, possible contamination and the inability to measure the low-energy β-emitter ^{33}P, especially in coastal environments with high P concentrations[1,8–10]. This study is, to our knowledge, the first to constrain the ^{32}P and ^{33}P input flux[6] and to simultaneously measure both these isotopes in various dissolved inorganic, organic and particulate pools.

Sampling was conducted in Wilkinson basin in the Gulf of Maine (42° 29.41′ N, 69° 45.02′ W) during four cruises in March, April, July and August 1997. This highly productive region supports one of the largest fisheries in North America[11]. Surface and deep particulate and total dissolved phosphorus (TDP) samples were collected by passing 4,000–6,000 l of sea water sequentially through a series of 10, 1.0 and 0.2 μm cartridge prefilters followed by cartridges packed with iron-impregnated polypropylene filters. These filters have been demonstrated to collect TDP with close to 100% efficiency[7]. Separate surface samples were collected for soluble reactive phosphorus (SRP), as defined by the molybdenum blue method[12], using acrilan filters and the technique developed by Lee *et al.*[9]. Plankton tows (nominally >102 μm) were collected from various depths and sieved through a 335-μm screen to collect different size classes. All samples were extensively purified to remove all other β-emitting radionuclides and counted using low-level liquid scintillation[6]. In March and April, deep-water P samples were taken just above the base of the mixed layer (defined by a change in density $\geqslant 0.125\,\mathrm{kg\,m^{-3}}$), whereas in July and August, deep-water samples were taken below both the mixed layer and the deep chlorophyll maximum.

The ratio of ^{33}P/^{32}P measured in rain at Portsmouth, NH and Woods Hole, MA was flux weighted over a 35 ± 3-day period before the April, July and August cruises and over a 14-day period before the March cruise. ^{33}P/^{32}P ratios averaged 0.82 ± 0.07 (Fig. 1, Table 1). Thus, any ratio higher than this value must be due to radioactive decay. A non-continuous model can be used to determine the relative age of phosphorus in any particular reservoir: $\tau_P = [\ln(R_P/R_S)]/(\lambda_{32} - \lambda_{33})$ where τ_P is the age of phosphorus in the product material, R_P and R_S are the ^{33}P/^{32}P ratio found in the product and source material, respectively, and λ_{32} and λ_{33} are the radioactive decay constants[5]. Using this model, phosphorus ages are resolved on timescales ranging from 1 to 100 days. In general, age estimate errors will increase with increasing ^{33}P/^{32}P ratios as P activities decrease over time.

In March, April and July, ratios of ^{33}P/^{32}P in particulate matter were similar between surface and deep waters, indicating rapid transport of sinking particulate material from the euphotic zone to depth (Fig. 1). In August, the activities in all particulate samples retrieved from deep waters were below detection, indicating that the source of sinking particulates had decreased. ^{33}P/^{32}P ratios in total dissolved and small particulate (<102 μm) surface pools measured during March, April and August were similar to those found in rain.

Supplementary Information 2.1:
Model for Mixing Chiral Assembly $\boldsymbol{2}_3$*·DEB*$_6$
with Achiral Assembly $\boldsymbol{6}_3$ *DEB*$_6$

1) Define two different conformations *M* en *P* for separate building blocks **2** and **6**.

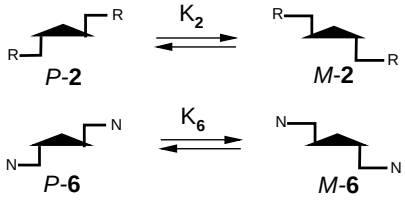

$$K_2 = \frac{[M\text{-}\mathbf{2}]}{[P\text{-}\mathbf{2}]} = e^{\frac{-2\Delta H_{R/S}}{RT}}$$

$$K_6 = \frac{[M\text{-}\mathbf{6}]}{[P\text{-}\mathbf{6}]} = 1$$

2) Incorporate *M/P*-conformations without change in energy into the assemblies.

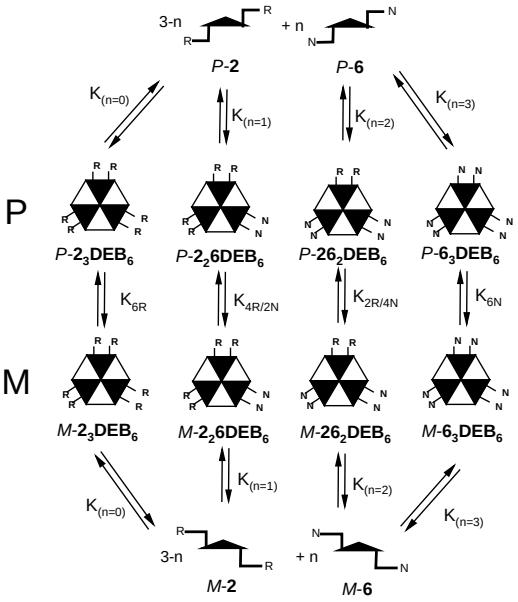

$$K_{6R} = \frac{[M\text{-}\mathbf{2_3DEB_6}]}{[P\text{-}\mathbf{2_3DEB_6}]} = \frac{[M\text{-}\mathbf{2}]^3}{[P\text{-}\mathbf{2}]^3} = (K_2)^3 = e^{\frac{-6\Delta H_{R/S}}{RT}}$$

$$K_{4R/2N} = \frac{[M\text{-}\mathbf{2_2 6DEB_6}]}{[P\text{-}\mathbf{2_2 6DEB_6}]} = \frac{[M\text{-}\mathbf{2}]^2[M\text{-}6]}{[M\text{-}\mathbf{2}]^2[M\text{-}6]} = (K_2)^2 K_6 = e^{\frac{-4\Delta H_{R/S}}{RT}}$$

$$K_{2R/4N} = \frac{[M\text{-}\mathbf{26_2DEB_6}]}{[P\text{-}\mathbf{26_2DEB_6}]} = \frac{[M\text{-}\mathbf{2}][M\text{-}6]^2}{[M\text{-}\mathbf{2}][M\text{-}6]^2} = K_2(K_6)^2 = e^{\frac{-2\Delta H_{R/S}}{RT}}$$

$$K_{6N} = \frac{[M\text{-}\mathbf{6_3DEB_6}]}{[P\text{-}\mathbf{6_3DEB_6}]} = \frac{[M\text{-}\mathbf{6}]^3}{[P\text{-}\mathbf{6}]^3} = (K_6)^3 = 1$$

N.B.: cooperativity between the chiral centres is not included in the model !!!

3) Curve fitting procedure (see attachment).

4) Calculate d.e.$_{6R}$, d.e.$_{4R/2N}$ and d.e.$_{2R/4N}$ from optimized $\Delta H_{R/S}$ values from curve fitting.

$$\text{d.e.}_{6R} = 100 \times \frac{(K_{6R} - 1)}{(K_{6R} + 1)}$$

$$\text{d.e.}_{4R/2N} = 100 \times \frac{(K_{4R/2N} - 1)}{(K_{4R/2N} + 1)}$$

$$\text{d.e.}_{2R/4N} = 100 \times \frac{(K_{2R/4N} - 1)}{(K_{2R/4N} + 1)}$$

Supplementary Information 2.2:
Curve Fitting Procedure for Mixed Assemblies $\mathbf{2_{3-n}6_n \bullet DEB_6}$ (n=0-3).

The equilibrium between assemblies and individual building blocks is described by

$$(3-n)\mathbf{2} + n\mathbf{6} \xleftrightarrow{K(n)} \mathbf{2}_{(3-n)}\mathbf{6}_n$$

$$K_{(n)} = \frac{[\mathbf{2}_{(3-n)}\mathbf{6}_n]}{[\mathbf{2}]^{(3-n)}[\mathbf{6}]^n}$$

$3K_{(n=0)}=K_{(n=1)}=K_{(n=2)}=3K_{(n=3)}$, as a result of the three possibilities of forming an assembly with composition **226** (**226**, **262**, and **622**) and **266** (**266**, **626**, and **662**). It is assumed that free components **2** and **6** are not present and therefore $K_{(n)}$ is assigned a value of 1E10. Assemblies with *P*-chirality are only formed from combinations of building blocks with *P*-conformation, *e.g. P*-**2** and *P*-**6**. The enthalpy of formation is identical for all assemblies (homomeric and heteromeric).

Based on these assumptions the mass balances for $[\mathbf{2}_{tot}]$ and $[\mathbf{6}_{tot}]$ are :

$$[\mathbf{2}]_{tot} = 3[P\text{-}\mathbf{2_3}\bullet\mathbf{DEB_6}] + 2[P\text{-}\mathbf{2_2 6}\bullet\mathbf{DEB_6}] + [P\text{-}\mathbf{26_2}\bullet\mathbf{DEB_6}] + 3[M\text{-}\mathbf{2_3}\bullet\mathbf{DEB_6}] + 2[M\text{-}\mathbf{2_2 6}\bullet\mathbf{DEB_6}] + [M\text{-}\mathbf{26_2}\bullet\mathbf{DEB_6}].$$

$$[\mathbf{2}]_{tot} = 3K_{(n=3)}[P\text{-}\mathbf{2}]^3 + 2K_{(n=2)}[P\text{-}\mathbf{2}]^2[P\text{-}\mathbf{6}] + K_{(n=1)}[P\text{-}\mathbf{2}][P\text{-}\mathbf{6}]^2 + 3K_{(n=3)}[M\text{-}\mathbf{2}]^3 + 2K_{(n=2)}[M\text{-}\mathbf{2}]^2[M\text{-}\mathbf{6}] + K_{(n=1)}[M\text{-}\mathbf{2}][M\text{-}\mathbf{6}]^2.$$

$$[\mathbf{2}]_{tot} = 3K_{(n=3)}[P\text{-}\mathbf{2}]^3 + 6K_{(n=3)}[P\text{-}\mathbf{2}]^2[P\text{-}\mathbf{6}] + 3K_{(n=3)}[P\text{-}\mathbf{2}][P\text{-}\mathbf{6}]^2 + 3K_{(n=3)}[M\text{-}\mathbf{2}]^3 + 6K_{(n=3)}[M\text{-}\mathbf{2}]^2[M\text{-}\mathbf{6}] + 3K_{(n=3)}[M\text{-}\mathbf{2}][M\text{-}\mathbf{6}]^2.$$

$$[\mathbf{2}]_{tot}/3K_{(n=3)} = [P\text{-}\mathbf{2}]^3 + 2[P\text{-}\mathbf{2}]^2[P\text{-}\mathbf{6}] + [P\text{-}\mathbf{2}][P\text{-}\mathbf{6}]^2 + [M\text{-}\mathbf{2}]^3 + 2[M\text{-}\mathbf{2}]^2[M\text{-}\mathbf{6}] + [M\text{-}\mathbf{2}][M\text{-}\mathbf{6}]^2.$$

$[M\text{-}\mathbf{2}] = K_{\mathbf{2}} \times [P\text{-}\mathbf{2}]$ and
$[M\text{-}\mathbf{6}] = K_{\mathbf{6}} \times [P\text{-}\mathbf{6}]$ gives:

$$[\mathbf{2}]_{tot}/3K_{(n=3)} = [P\text{-}\mathbf{2}]^3(1+K_2{}^3) + 2[P\text{-}\mathbf{2}]^2[P\text{-}\mathbf{6}](1+K_2{}^2K_{\mathbf{6}}) + [P\text{-}\mathbf{2}][P\text{-}\mathbf{6}]^2(1+K_2K_{\mathbf{6}}{}^2).$$

With $K_{\mathbf{6}} = 1$:

$$= [P\text{-}\mathbf{2}]^3(1+K_2{}^3) + 2[P\text{-}\mathbf{2}]^2[P\text{-}\mathbf{6}](1+K_2{}^2) + [P\text{-}\mathbf{2}][P\text{-}\mathbf{6}]^2(1+K_2).$$

This equation expresses [*P*-**6**] as a function of K_2 and [*P*-**2**].

$$[\mathbf{6}]_{tot} = 3[P\text{-}\mathbf{6_3}\bullet\mathbf{DEB_6}] + 2[P\text{-}\mathbf{26_2}\bullet\mathbf{DEB_6}] + [P\text{-}\mathbf{2_2 6}\bullet\mathbf{DEB_6}] + 3[M\text{-}\mathbf{6_3}\bullet\mathbf{DEB_6}] + 2[M\text{-}\mathbf{26_2}\bullet\mathbf{DEB_6}] + [M\text{-}\mathbf{2_2 6}\bullet\mathbf{DEB_6}].$$

$$[\mathbf{6}]_{tot} = 3K_{(n=0)}[P\text{-}\mathbf{6}]^3 + 2K_{(n=1)}[P\text{-}\mathbf{2}][P\text{-}\mathbf{6}]^2 + K_{(n=2)}[P\text{-}\mathbf{2}]^2[P\text{-}\mathbf{6}] +$$

$$3K_{(n=0)}[M\text{-}\mathbf{6}]^3 + 2K_{(n=1)}[M\text{-}\mathbf{2}][M\text{-}\mathbf{6}]^2 + K_{(n=2)}[M\text{-}\mathbf{2}]^2[M\text{-}\mathbf{6}].$$

$$[\mathbf{6}]_{tot} = 3K_{(n=0)}[P\text{-}\mathbf{6}]^3 + 6K_{(n=0)}[P\text{-}\mathbf{2}][P\text{-}\mathbf{6}]^2 + 3K_{(n=0)}[P\text{-}\mathbf{2}]^2[P\text{-}\mathbf{6}] + 3K_{(n=0)}[M\text{-}\mathbf{6}]^3 + 6K_{(n=0)}[M\text{-}\mathbf{2}][M\text{-}\mathbf{6}]^2 + 3K_{(n=0)}[M\text{-}\mathbf{2}]^2[M\text{-}\mathbf{6}].$$

$$[\mathbf{6}]_{tot}/3K_{(n=0)} = [P\text{-}\mathbf{6}]^3 + 2[P\text{-}\mathbf{2}][P\text{-}\mathbf{6}]^2 + [P\text{-}\mathbf{2}]^2[P\text{-}\mathbf{6}] + [M\text{-}\mathbf{6}]^3 + 2[M\text{-}\mathbf{2}][M\text{-}\mathbf{6}]^2 + [M\text{-}\mathbf{2}]^2[M\text{-}\mathbf{6}].$$

$[M\text{-}\mathbf{2}] = K_{\mathbf{2}} \times [P\text{-}\mathbf{2}]$ and
$[M\text{-}\mathbf{6}] = K_{\mathbf{6}} \times [P\text{-}\mathbf{6}]$ gives:

$$[\mathbf{6}]_{tot}/3K_{(n=0)} = [P\text{-}\mathbf{6}]^3(1+K_{\mathbf{6}}^3) + 2[P\text{-}\mathbf{6}]^2[P\text{-}\mathbf{2}](1+K_{\mathbf{6}}^2K_{\mathbf{2}}) + [P\text{-}\mathbf{6}][P\text{-}\mathbf{2}]^2(1+K_{\mathbf{6}}K_{\mathbf{2}}^2).$$

With $K_{\mathbf{6}} = 1$:

$$= 2[P\text{-}\mathbf{6}]^3 + 2[P\text{-}\mathbf{6}]^2[P\text{-}\mathbf{2}](1+K_{\mathbf{2}}) + [P\text{-}\mathbf{6}][P\text{-}\mathbf{2}]^2(1+K_{\mathbf{2}}^2).$$

This equation expresses [*P*-**2**] as a function of $K_{\mathbf{2}}$ and [*P*-**6**]

From these two equations [*P*-**2**] and [*P*-**6**] can be numerically calculated for a specific value of $K_{\mathbf{2}}$.

From [*P*-**2**] and [*P*-**6**] a CD-signal is calculated using:

$[P\text{-}\mathbf{2_3{\bullet}DEB_6}] = K_{(n=3)}[P\text{-}\mathbf{2}]^3$
$[M\text{-}\mathbf{2_3{\bullet}DEB_6}] = K_{(n=3)}[M\text{-}\mathbf{2}]^3 = K_{(n=3)}K_{\mathbf{2}}^3[P\text{-}\mathbf{2}]^3 = K_{\mathbf{2}}^3[P\text{-}\mathbf{2_3{\bullet}DEB_6}]$
$[P\text{-}\mathbf{2_2 6{\bullet}DEB_6}] = 3K_{(n=3)}[P\text{-}\mathbf{2}]^2[P\text{-}\mathbf{6}]$
$[M\text{-}\mathbf{2_2 6{\bullet}DEB_6}] = 3K_{(n=3)}[M\text{-}\mathbf{2}]^2[M\text{-}\mathbf{6}] = 3K_{(n=3)}K_{\mathbf{2}}^2[P\text{-}\mathbf{2}]^2K_{\mathbf{6}}[P\text{-}\mathbf{6}] = K_{\mathbf{2}}^2[P\text{-}\mathbf{2_2 6{\bullet}DEB_6}]$
$[P\text{-}\mathbf{26_2{\bullet}DEB_6}] = 3K_{(n=3)}[P\text{-}\mathbf{2}][P\text{-}\mathbf{6}]^2$
$[M\text{-}\mathbf{26_2{\bullet}DEB_6}] = 3K_{(n=3)}[M\text{-}\mathbf{2}][M\text{-}\mathbf{6}]^2 = 3K_{(n=3)}K_{\mathbf{2}}[P\text{-}\mathbf{2}]K_{\mathbf{6}}^2[P\text{-}\mathbf{6}]^2 = K_{\mathbf{2}}[P\text{-}\mathbf{26_2{\bullet}DEB_6}]$

resulting in:

$$\Delta\varepsilon_{calc.} = SF\ \frac{[M\text{-}\mathbf{2_3{\bullet}DEB_6}]-[P\text{-}\mathbf{2_3{\bullet}DEB_6}]+[M\text{-}\mathbf{2_2 6{\bullet}DEB_6}]-[P\text{-}\mathbf{2_2 6{\bullet}DEB_6}]+[M\text{-}\mathbf{26_2{\bullet}DEB_6}]-[P\text{-}\mathbf{26_2{\bullet}DEB_6}]}{[M\text{-}\mathbf{2_3{\bullet}DEB_6}]+[P\text{-}\mathbf{2_3{\bullet}DEB_6}]+[M\text{-}\mathbf{2_2 6{\bullet}DEB_6}]+[P\text{-}\mathbf{2_2 6{\bullet}DEB_6}]+[M\text{-}\mathbf{26_2{\bullet}DEB_6}]+[P\text{-}\mathbf{26_2{\bullet}DEB_6}]}$$

$$= \frac{d.e._{6R}[\mathbf{2_3{\bullet}DEB_6}] + d.e._{4R/2N}[\mathbf{2_2 6{\bullet}DEB_6}] + d.e._{2R/4N}[\mathbf{26_2{\bullet}DEB_6}])}{(\Sigma[\mathbf{2_{3-n}6_n{\bullet}DEB_6}])} \times \Delta\varepsilon_{(\mathbf{23{\bullet}DEB6})}$$

SF: Scaling Factor

The experimental CD-curve can now be fitted by variation of $K_{\mathbf{2}}$ using least rms fit analysis. ([*P*-**2**] and [*P*-**6**] are numerically solved for each $K_{\mathbf{2}}$ in a subroutine).

Supplementary Material 3.1:
Model for Mixing Chiral Assemblies ***2***$_3$*·DEB*$_6$ *and* ***3***$_3$*·DEB*$_6$

1) Define two different conformations *M* en *P* for separate building blocks **2** and **3**.

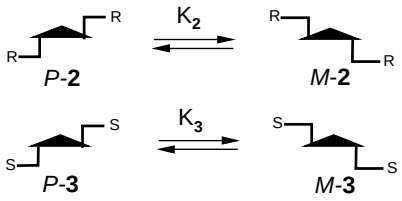

$$K_2 = \frac{[M\text{-}\mathbf{2}]}{[P\text{-}\mathbf{2}]} = 1/K_3 = e^{\frac{-2\Delta H_{R/S}}{RT}}$$

$$K_3 = \frac{[M\text{-}\mathbf{3}]}{[P\text{-}\mathbf{3}]} = 1/K_2 = e^{\frac{2\Delta H_{R/S}}{RT}}$$

2) Incorporate *M/P*-conformations without change in energy into the assemblies.

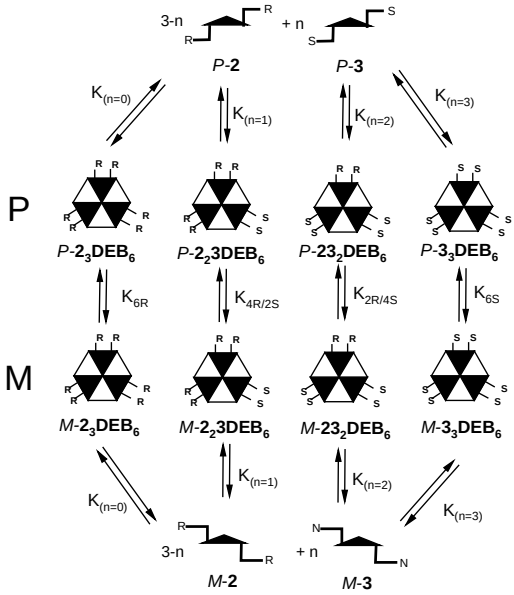

$$K_{6R} = \frac{[M\text{-}\mathbf{2_3DEB_6}]}{[P\text{-}\mathbf{2_3DEB_6}]} = \frac{[M\text{-}\mathbf{2}]^3}{[P\text{-}\mathbf{2}]^3} = (K_2)^3 = e^{\frac{-6\Delta H_{R/S}}{RT}}$$

$$K_{4R/2S} = \frac{[M\text{-}\mathbf{2_23DEB_6}]}{[P\text{-}\mathbf{2_23DEB_6}]} = \frac{[M\text{-}\mathbf{2}]^2[M\text{-}\mathbf{3}]}{[M\text{-}\mathbf{2}]^2[M\text{-}\mathbf{3}]} = (K_2)^2K_3 = e^{\frac{-2\Delta H_{R/S}}{RT}}$$

$$K_{2R/4S} = \frac{[M\text{-}\mathbf{23_2DEB_6}]}{[P\text{-}\mathbf{23_2DEB_6}]} = \frac{[M\text{-}\mathbf{2}][M\text{-}\mathbf{3}]^2}{[M\text{-}\mathbf{2}][M\text{-}\mathbf{3}]^2} = K_2(K_3)^2 = e^{\frac{2\Delta H_{R/S}}{RT}}$$

$$K_{6S} = \frac{[M\text{-}\mathbf{3_3DEB_6}]}{[P\text{-}\mathbf{3_3DEB_6}]} = \frac{[M\text{-}\mathbf{3}]^3}{[P\text{-}\mathbf{3}]^3} = (K_3)^3 = e^{\frac{6\Delta H_{R/S}}{RT}}$$

N.B.: cooperativity between the chiral centres is not included in the model !!!

3) Curve fitting procedure (see attachment).

4) Calculate curves and composition of the mixture.

Supplementary Information 3.2:
Curve Fitting Procedure for Mixed Assemblies $\mathbf{2}_{3-n}\mathbf{3}_n\bullet\mathbf{DEB}_6$ (n=0-3).

The equilibrium between assemblies and individual building blocks is described by

$$(3-n)\mathbf{2} + n\mathbf{3} \xleftrightarrow{K(n)} \mathbf{2}_{(3-n)}\mathbf{3}_n$$

$$K_{(n)} = \frac{[\mathbf{2}_{(3-n)}\mathbf{3}_n]}{[\mathbf{2}]^{(3-n)}[\mathbf{3}]^n}$$

$3K_{(n=0)}=K_{(n=1)}=K_{(n=2)}=3K_{(n=3)}$, as a result of the three possibilities of forming an assembly with composition **223** (**223**, **232**, and **322**) and **233** (**233**, **323**, and **332**). It is assumed that free components **2** and **3** are not present and therefore $K_{(n)}$ is assigned a value of 1E10. Assemblies with *P*-chirality are only formed from combinations of building blocks with *P*-conformation, *e.g. P*-**2** and *P*-**3**. The enthalpy of formation is identical for all assemblies (homomeric and heteromeric).

Based on these assumptions the mass balances for $[\mathbf{2}_{tot}]$ and $[\mathbf{3}_{tot}]$ are :

$$[\mathbf{2}]_{tot} = 3[P\text{-}\mathbf{2}_3\bullet\mathbf{DEB}_6] + 2[P\text{-}\mathbf{2}_2\mathbf{3}\bullet\mathbf{DEB}_6] + [P\text{-}\mathbf{23}_2\bullet\mathbf{DEB}_6] + 3[M\text{-}\mathbf{2}_3\bullet\mathbf{DEB}_6] + 2[M\text{-}\mathbf{2}_2\mathbf{3}\bullet\mathbf{DEB}_6] + [M\text{-}\mathbf{23}_2\bullet\mathbf{DEB}_6].$$

$$[\mathbf{2}]_{tot} = 3K_{(n=3)}[P\text{-}\mathbf{2}]^3 + 2K_{(n=2)}[P\text{-}\mathbf{2}]^2[P\text{-}\mathbf{3}] + K_{(n=1)}[P\text{-}\mathbf{2}][P\text{-}\mathbf{3}]^2 + 3K_{(n=3)}[M\text{-}\mathbf{2}]^3 + 2K_{(n=2)}[M\text{-}\mathbf{2}]^2[M\text{-}\mathbf{3}] + K_{(n=1)}[M\text{-}\mathbf{2}][M\text{-}\mathbf{3}]^2.$$

$$[\mathbf{2}]_{tot} = 3K_{(n=3)}[P\text{-}\mathbf{2}]^3 + 6K_{(n=3)}[P\text{-}\mathbf{2}]^2[P\text{-}\mathbf{3}] + 3K_{(n=3)}[P\text{-}\mathbf{2}][P\text{-}\mathbf{3}]^2 + 3K_{(n=3)}[M\text{-}\mathbf{2}]^3 + 6K_{(n=3)}[M\text{-}\mathbf{2}]^2[M\text{-}\mathbf{3}] + 3K_{(n=3)}[M\text{-}\mathbf{2}][M\text{-}\mathbf{3}]^2.$$

$$[\mathbf{2}]_{tot}/3K_{(n=3)} = [P\text{-}\mathbf{2}]^3 + 2[P\text{-}\mathbf{2}]^2[P\text{-}\mathbf{3}] + [P\text{-}\mathbf{2}][P\text{-}\mathbf{3}]^2 + [M\text{-}\mathbf{2}]^3 + 2[M\text{-}\mathbf{2}]^2[M\text{-}\mathbf{3}] + [M\text{-}\mathbf{2}][M\text{-}\mathbf{3}]^2.$$

$[M\text{-}\mathbf{2}] = K_{\mathbf{2}} \times [P\text{-}\mathbf{2}]$ and
$[M\text{-}\mathbf{3}] = K_{\mathbf{3}} \times [P\text{-}\mathbf{3}]$ gives:

$$[\mathbf{2}]_{tot}/3K_{(n=3)} = [P\text{-}\mathbf{2}]^3(1+K_2{}^3) + 2[P\text{-}\mathbf{2}]^2[P\text{-}\mathbf{3}](1+K_2{}^2K_3) + [P\text{-}\mathbf{2}][P\text{-}\mathbf{3}]^2(1+K_2K_3{}^2).$$

With $K_3 = 1/K_2$:

$$= [P\text{-}\mathbf{2}]^3(1+K_2{}^3) + 2[P\text{-}\mathbf{2}]^2[P\text{-}\mathbf{3}](1+K_2) + [P\text{-}\mathbf{2}][P\text{-}\mathbf{3}]^2(1+1/K_2).$$

This equation expresses [*P*-**3**] as a function of K_2 and [*P*-**2**].

$$[\mathbf{3}]_{tot} = 3[P\text{-}\mathbf{3}_3\bullet\mathbf{DEB}_6] + 2[P\text{-}\mathbf{23}_2\bullet\mathbf{DEB}_6] + [P\text{-}\mathbf{2}_2\mathbf{3}\bullet\mathbf{DEB}_6] + 3[M\text{-}\mathbf{3}_3\bullet\mathbf{DEB}_6] + 2[M\text{-}\mathbf{23}_2\bullet\mathbf{DEB}_6] + [M\text{-}\mathbf{2}_2\mathbf{3}\bullet\mathbf{DEB}_6].$$

$$[\mathbf{3}]_{tot} = 3K_{(n=0)}[P\text{-}\mathbf{3}]^3 + 2K_{(n=1)}[P\text{-}\mathbf{2}][P\text{-}\mathbf{3}]^2 + K_{(n=2)}[P\text{-}\mathbf{2}]^2[P\text{-}\mathbf{3}] +$$

$$3K_{(n=0)}[M\text{-}\mathbf{3}]^3 + 2K_{(n=1)}[M\text{-}\mathbf{2}][M\text{-}\mathbf{3}]^2 + K_{(n=2)}[M\text{-}\mathbf{2}]^2[M\text{-}\mathbf{3}].$$

$$[\mathbf{3}]_{tot} = 3K_{(n=0)}[P\text{-}\mathbf{3}]^3 + 6K_{(n=0)}[P\text{-}\mathbf{2}][P\text{-}\mathbf{3}]^2 + 3K_{(n=0)}[P\text{-}\mathbf{2}]^2[P\text{-}\mathbf{3}] + 3K_{(n=0)}[M\text{-}\mathbf{3}]^3 + 6K_{(n=0)}[M\text{-}\mathbf{2}][M\text{-}\mathbf{3}]^2 + 3K_{(n=0)}[M\text{-}\mathbf{2}]^2[M\text{-}\mathbf{3}].$$

$$[\mathbf{3}]_{tot}/3K_{(n=0)} = [P\text{-}\mathbf{3}]^3 + 2[P\text{-}\mathbf{2}][P\text{-}\mathbf{3}]^2 + [P\text{-}\mathbf{2}]^2[P\text{-}\mathbf{3}] + [M\text{-}\mathbf{3}]^3 + 2[M\text{-}\mathbf{2}][M\text{-}\mathbf{3}]^2 + [M\text{-}\mathbf{2}]^2[M\text{-}\mathbf{3}].$$

$[M\text{-}\mathbf{2}] = K_{\mathbf{2}} \times [P\text{-}\mathbf{2}]$ and
$[M\text{-}\mathbf{3}] = K_{\mathbf{3}} \times [P\text{-}\mathbf{3}]$ gives:

$$[\mathbf{3}]_{tot}/3K_{(n=0)} = [P\text{-}\mathbf{3}]^3(1+K_{\mathbf{3}}^3) + 2[P\text{-}\mathbf{3}]^2[P\text{-}\mathbf{2}](1+K_{\mathbf{3}}^2K_{\mathbf{2}}) + [P\text{-}\mathbf{3}][P\text{-}\mathbf{2}]^2(1+K_{\mathbf{3}}K_{\mathbf{2}}^2).$$

With $K_{\mathbf{3}} = 1/K_{\mathbf{2}}$:

$$= [P\text{-}\mathbf{3}]^3(1+1/K_{\mathbf{2}}^3) + 2[P\text{-}\mathbf{3}]^2[P\text{-}\mathbf{2}](1+1/K_{\mathbf{2}}) + [P\text{-}\mathbf{3}][P\text{-}\mathbf{2}]^2(1+K_{\mathbf{2}}).$$

This equation expresses [*P*-**2**] as a function of $K_{\mathbf{2}}$ and [*P*-**3**].

From these two equations [*P*-**2**] and [*P*-**3**] can be calculated numerically for a specific value of $K_{\mathbf{2}}$.

From [*P*-**2**] and [*P*-**3**] a CD-signal is calculated using:

$[P\text{-}\mathbf{2_3}\bullet\mathbf{DEB_6}] = K_{(n=3)}[P\text{-}\mathbf{2}]^3$
$[M\text{-}\mathbf{2_3}\bullet\mathbf{DEB_6}] = K_{(n=3)}[M\text{-}\mathbf{2}]^3 = K_{(n=3)}K_{\mathbf{2}}^3[P\text{-}\mathbf{2}]^3 = K_{\mathbf{2}}^3[P\text{-}\mathbf{2_3}\bullet\mathbf{DEB_6}]$
$[P\text{-}\mathbf{2_2 3}\bullet\mathbf{DEB_6}] = 3K_{(n=3)}[P\text{-}\mathbf{2}]^2[P\text{-}\mathbf{3}]$
$[M\text{-}\mathbf{2_2 3}\bullet\mathbf{DEB_6}] = 3K_{(n=3)}[M\text{-}\mathbf{2}]^2[M\text{-}\mathbf{3}] = 3K_{(n=3)}K_{\mathbf{2}}^2[P\text{-}\mathbf{2}]^2K_{\mathbf{3}}[P\text{-}\mathbf{3}] = K_{\mathbf{2}}[P\text{-}\mathbf{2_2 3}\bullet\mathbf{DEB_6}]$
$[P\text{-}\mathbf{23_2}\bullet\mathbf{DEB_6}] = 3K_{(n=3)}[P\text{-}\mathbf{2}][P\text{-}\mathbf{3}]^2$
$[M\text{-}\mathbf{23_2}\bullet\mathbf{DEB_6}] = 3K_{(n=3)}[M\text{-}\mathbf{2}][M\text{-}\mathbf{3}]^2 = 3K_{(n=3)}K_{\mathbf{2}}[P\text{-}\mathbf{2}]K_{\mathbf{3}}^2[P\text{-}\mathbf{3}]^2 = (1/K_{\mathbf{2}})[P\text{-}\mathbf{23_2}\bullet\mathbf{DEB_6}]$
$[P\text{-}\mathbf{3_3}\bullet\mathbf{DEB_6}] = K_{(n=3)}[P\text{-}\mathbf{3}]^3$
$[M\text{-}\mathbf{3_3}\bullet\mathbf{DEB_6}] = K_{(n=3)}[M\text{-}\mathbf{3}]^3 = K_{(n=3)}K_{\mathbf{3}}^3[P\text{-}\mathbf{3}]^3 = (1/K_{\mathbf{2}})^3[P\text{-}\mathbf{3_3}\bullet\mathbf{DEB_6}]$

resulting in:

$$\Delta\varepsilon_{calc.} = SF\ ([M\text{-}\mathbf{2_3}\bullet\mathbf{DEB_6}]\text{-}[P\text{-}\mathbf{2_3}\bullet\mathbf{DEB_6}]+[M\text{-}\mathbf{2_2 3}\bullet\mathbf{DEB_6}]\text{-}[P\text{-}\mathbf{2_2 3}\bullet\mathbf{DEB_6}]+ [M\text{-}\mathbf{23_2}\bullet\mathbf{DEB_6}]\text{-}[P\text{-}\mathbf{23_2}\bullet\mathbf{DEB_6}]+[M\text{-}\mathbf{3_3}\bullet\mathbf{DEB_6}]\text{-}[P\text{-}\mathbf{3_3}\bullet\mathbf{DEB_6}]+) / ([M\text{-}\mathbf{2_3}\bullet\mathbf{DEB_6}]+[P\text{-}\mathbf{2_3}\bullet\mathbf{DEB_6}]+[M\text{-}\mathbf{2_2 3}\bullet\mathbf{DEB_6}]+[P\text{-}\mathbf{2_2 3}\bullet\mathbf{DEB_6}]+ [M\text{-}\mathbf{23_2}\bullet\mathbf{DEB_6}]+[P\text{-}\mathbf{23_2}\bullet\mathbf{DEB_6}]+[M\text{-}\mathbf{3_3}\bullet\mathbf{DEB_6}]+[P\text{-}\mathbf{3_3}\bullet\mathbf{DEB_6}])$$

$$= SF\ \frac{(d.e._{6R}[\mathbf{2_3}\bullet\mathbf{DEB_6}] + d.e._{4R/2S}[\mathbf{2_2 3}\bullet\mathbf{DEB_6}] + d.e._{2R/4S}[\mathbf{23_2}\bullet\mathbf{DEB_6}] + d.e._{6S}[\mathbf{3_3}\bullet\mathbf{DEB_6}])}{\Sigma_{(n=0\text{-}3)}[\mathbf{2_{3-n}3_n}\bullet\mathbf{DEB_6}]} \times \Delta\varepsilon_{(\mathbf{23}\bullet\mathbf{DE}}$$

SF: Scaling Factor

The experimental CD-curve can now be fitted by variation of $K_{\mathbf{2}}$. ([*P*-**2**] and [*P*-**3**] are numerically solved for each $K_{\mathbf{2}}$ in a subroutine) using least rms fit analysis.